Minimizing Defect on Ti Thin Film Laser Ablation using Square Flat-top NIR Femtosecond Laser for Thin Film Transistor of μ-LED Repair

Junha Choi[1,2], Kwangwoo Cho[1,2], Seok-Young Ji[2], Won-Seok Chang[1,2], Sunghwan Chang[2], and Sung-Hak Cho[*,1,2]

[1]*Department of Nano-Mechatronics, Korea University of Science and Technology, South Korea*
[2]*Department of Nano-manufacturing Technology, Nano-Convergence Manufacturing Systems Research Division, Korea Institute of Machinery and Materials, South Korea*
[*]*Corresponding author's e-mail: shcho@kimm.re.kr*

In this paper, we report on the ablation of Ti thin films with a thickness of 100 nm, while minimizing defects. Ti thin films are used in the TFT of μ-LEDs, and repair processing is required to increase the production yield of μ-LEDs. The repair process involves selectively ablating specific regions with a femtosecond laser, which must be done with precision to ensure proper TFT operation. Precise ablation means that defects, such as burrs, ripples, and substrate ablation, do not occur. To implement minimizing defects, we conducted COMSOL Multiphysics simulations using both Gaussian and flat-top beams. We irradiated the sample with a laser under various conditions, including pulse fluence, number of pulses, and beam deformation, and assessed the resulting ablation quality. Through careful selection of the laser conditions, which include flat-top beam with 0.28 J/cm^2 fluence and 7 pulses, we were able to minimize burrs, ripples, and substrate ablation, resulting in neat and minimizing defect of 100 nm Ti ablation.

DOI: 10.2961/jlmn.2023.03.2005

Keywords: femtosecond laser ablation, titanium thin film, flat-top beam, burr, ripple

1. Introduction

μ-LED displays have emerged as a promising next-generation display technology, due to their high contrast, fast response speed, accurate color representation, wide viewing angle, and high power efficiency. These features outperform existing LCD and OLED displays. However, despite their potential benefits, current μ-LED displays are not yet mass-produced due to high production costs and low yield rates [1-3]. In particular, manufacturing μ-LED displays requires advanced repair processing technology to selectively remove defective laminated multifunctional thin films and increase production yield.

Titanium (Ti) is a widely used semiconductor circuit bonding material in optoelectronic devices such as flat panel displays, touch panels, solar cells, and organic light-emitting devices (OLEDs). Specifically, it is an important material used as the pad electrode and gate electrode in the laminated structure of the thin film transistor (TFT), which is a μ-LED display driver [4]. The pad electrode is essential for connecting the transistor to other electronic components and integrating it into larger electronic systems. In the TFT part, μ-LED repair methods can be broadly divided into two categories. The first method involves connecting through an additional deposition process in a separate section that was incorrectly deposited and should be connected during the TFT circuit production. The second method involves partially processing and separating the parts that were incorrectly deposited and connected during TFT circuit manufacturing. Repairing the TFT part can significantly increase the yield of μ-LEDs, but it must not damage or affect the peripheral parts or underlying materials. Damage and effects generated during repair may become a problem during subsequent thin film deposition and processing. Among the two repair processes, we focused on partially processing using a femtosecond laser, and minimized defects in repair to selectively process Ti only accurately and neatly.

With the advent of high intensity femtosecond lasers, multiple materials and high intensity lasers have become important areas of interest. Laser ablation is a technique that uses laser energy to remove a target material from a substrate, allowing for precise patterning of the desired area through local heating and material removal [5,6]. Generally, ultrashort pulse lasers cause fewer thermal defects in materials compared to long pulse lasers [7]. However, even when using ultrashort pulse lasers for laser ablation, unintended shape defects such as cracks, particles, burrs, and ripples can still occur [8-13]. These defects arise under different conditions depending on the femtosecond laser applied to the material. To selectively, accurately, and neatly process a specific region of Ti for TFT repair, it is necessary to accurately understand the conditions that generate defects and to process the corresponding material under conditions in which no defects occur.

The goal of this study is to process Ti thin film in a specific area with minimal defects. To achieve this, we utilized a flat-top beam instead of a Gaussian beam [14,15]. Machining a specific area requires a homogeneous processing surface. While femtosecond lasers for Ti have been extensively studied for processing and ablation, most studies have used Gaussian beams, and there is limited research on achieving high reproducibility for both processing area and depth. However, the flat-top beam provides a homogeneous processing area through a homogeneous square beam intensity and enables homogeneous depth processing. We also investigate in detail the characteristics of defects through thermal distribution and morphology analysis under specific laser

conditions. The type of defects varies depending on the laser conditions and can be minimized by optimizing the laser parameters. As a result, it is possible to minimize defects for TFT repair of μ-LEDs and achieve perfect Ti thin film processing with a homogeneous area and depth.

2. Methods and Materials

In this experiment, a femtosecond laser with a wavelength of 1026 nm, pulse duration of 190 fs, repetition rate of 1 kHz, and a raw beam diameter of 4 mm was used to process a 100 nm thin film of Ti deposited on sodalime glass (Thickness : 1 mm). The Ti film was deposited using an e-beam evaporator (KVET-C500200, Korea Vacuum). The raw beam had a Gaussian beam profile. The beam path, as shown in figure 1, was designed to use Gaussian and flat-top beams. A flat-top beam is a beam with a square beam profile and uniform intensity [14,15]. Figure 1(b) shows the method of focusing the laser on the target sample using a Gaussian beam. The objective lens (OB, Mitutoyo, M Plan Apo NIR 50X, NA 0.42) was used to focus the laser on the target sample. Figure 1(c) shows the method of focusing the laser on the target sample using a flat-top beam. To create a flat-top beam, a mechanical slit and tube lens were used. The mechanical slit cut the low intensity periphery of the Gaussian beam, leaving only the high intensity center. The tube lens adjusted the beam focusing position. In this case, the beam was focused slightly above the sample surface. This is conducted to defocus the beam in order to achieve a uniform beam intensity, a square shaped beam with clear corners, and to transmit the slit image through the OB while eliminating distortion aberration. The OB used in figure 1(c) was the same as that used in figure 1(b). The beam passing through the OB was slightly defocused to obtain a homogeneous, square beam profile with clear edges. The beam profiles of the Gaussian and flat-top beams are confirmed in figures 1(b) and 1(c). In the beam profile of figure 1(c), there is a peripheral part of weak intensity outside the square due to the diffraction phenomenon. However, since the surrounding area had significantly lower intensity, diffraction did not significantly impact the film processing. After processing, the Ti thin films were analyzed using confocal microscopy (VK-X1000 Series, KEYENCE), FE-SEM (Sirion, FEI), and atomic force microscopy (AFM, XE-100, PSIA). These analyses were conducted to evaluate the surface morphology and quality of the processed films. The processed Ti thin films are intended to be applied to the Ti thin layer used in the TFT of the μ-LED [4].

3. Results and Discussion

Micromachining using lasers can result in various forms of ablation depending on the laser conditions, such as wavelength, fluence, pulse duration, repetition rate, and number of pulses [16]. However, additional defects are often generated during the ablation process [8-13]. In this study, we investigated the changes in defects that occur when micromachining is performed with Gaussian beams and flat-top beams. Figure 2 shows SEM images of a Ti thin film after being irradiated with 100 pulses while increasing the fluence with a Gaussian beam. The image reveals defects such as ripples, burrs, and glass processing. Figure 2a shows an image of 100 pulses irradiated with a fluence of 0.047 J/cm^2, which exhibits structures in the vertical direction known as ripples. Ripples are generated by the interference of the surface plasmon induced by the first incident pulse and the subsequent incident pulse [11-13]. Therefore, the ripple is affected by the fluence of the laser, the number of pulses, the repetition rate, and the pulse duration, and is generated from the fluence near the ablation threshold [11-13]. Since 100 pulses were irradiated in this case, ripples were easily generated [17,18]. Figures 2b and c show images of fluences 0.114 J/cm^2 and 0.28 J/cm^2, respectively. A Gaussian beam has high intensity in the center and low intensity in the periphery [19]. Therefore, fluence similar to the ablation threshold was formed in the peripheral area, resulting in the formation of both ripples and burrs. Burrs are formed due to the tensile strength induced by the high temperature in the

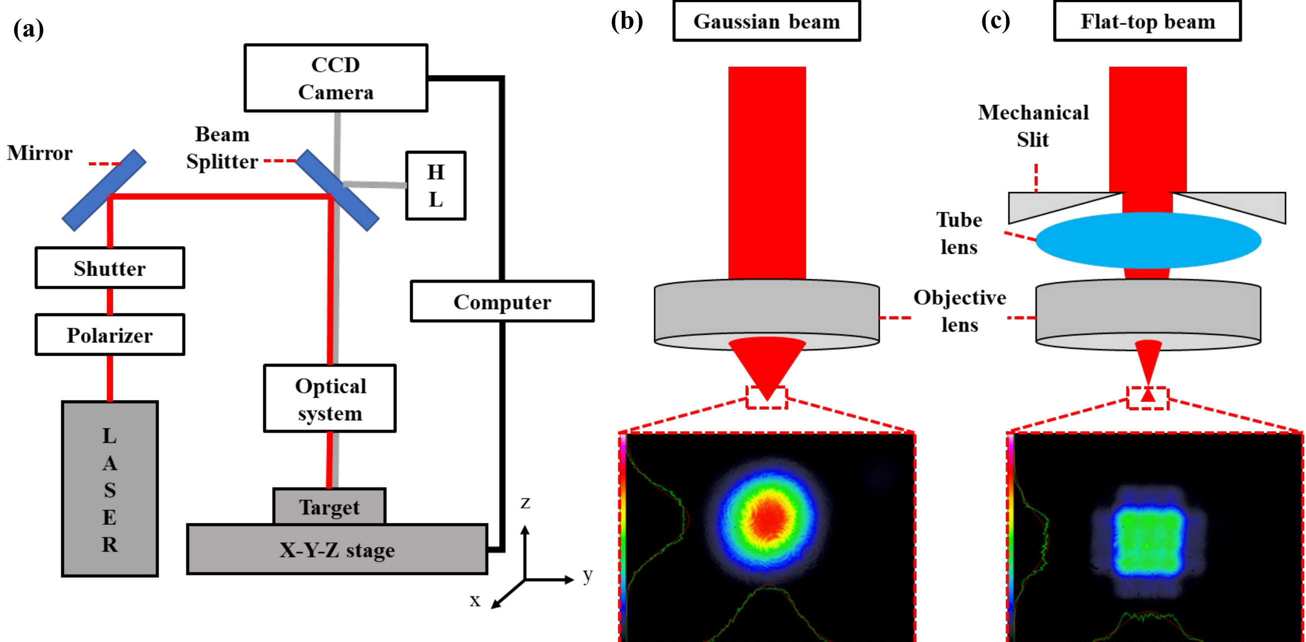

Fig. 1 Schematic image of femtosecond laser ablation setup: (a) Optical beam path of femtosecond laser, (b) Gaussian beam path and beam profile, (c) Flat-top beam path and beam profile (HL : Halogen lamp).

center of the sample irradiated with the Gaussian beam. Ti in the solid and liquid state is pushed to the periphery during the laser processing of coulomb explosion, fragmentation, phase explosion, and spallation [20-23]. Figure 3a shows the representative morphology of the burr formation, which is a hill higher than the surface at the boundary of the processing area. Figure 2d is an image irradiated with a fluence of 0.6 J/cm^2. In this case, not only Ti but also the substrate area, which is made of glass, was ablated due to the high pulse fluence. Since the Gaussian beam profile has high intensity in the center, glass ablation did not occur in the periphery but only in the center [19]. Figure 3b shows the burr height of figures 2b, c, and d. Figure 3c shows the ablation depth of figures 2b, c, and d. Figure 3d shows the ablation diameter of figures 2a, b, c, and d. In figures 2 and 3, ripple, burr, and substrate processing defects caused by laser processing can be observed. These defects can be problematic when using the thin film as a TFT. Therefore, it is essential to minimize the defects as much as possible to achieve clean processing. In the case of ripple, the thin film should be processed using the minimum pulse to suppress the effect of ripple, which is

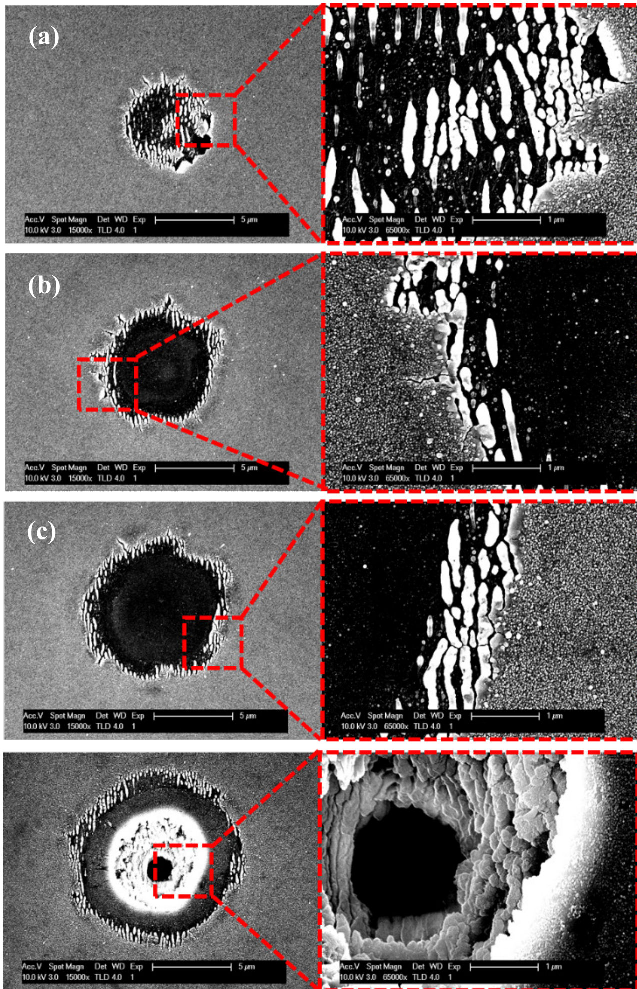

Fig. 2 SEM images of defects. Gaussian beam with increasing fluence was irradiated to Ti 100 nm film deposited on glass substrate. (a) Ripple, 100 pulses of 0.047 J/cm^2 fluence were irradiated (b) Ripple and burr, 100 pulses of 0.114 J/cm^2 fluence were irradiated (c) Ripple and burr, 100 pulses of 0.28 J/cm^2 fluence were irradiated (d) Ripple and burr, 100 pulses of 0.6 J/cm^2 fluence were irradiated.

generated by the interference of the surface plasmon present on the sample surface and the irradiated laser [17,18]. In the case of a burr, it is necessary to avoid generating strong tensile strength through beam-shaped deformation and to use appropriately low fluence pulses [20-23]. In the case of glass processing, it is caused by high fluence. Therefore, the Ti thin film must be ablated using appropriately low fluence pulses.

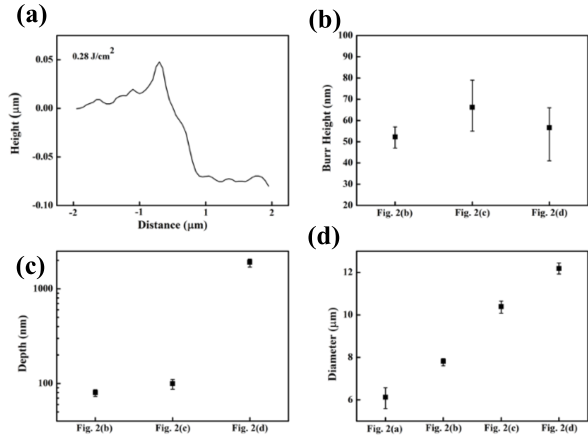

Fig. 3 Ablation characteristic and defects analysis of figure 2. Defects were analyzed by confocal microscopy. (a) Representative morphology of burr induced by Gaussian beam. Burr is a hill higher than sample surface (b) Burr height of figure 2b, c, and d. (c) Depth of figure 2b, c, and d. (d) Diameter of figure 2a, b, c, and d.

Figure 4 illustrates the heat distribution generated when a 100 nm Ti film is irradiated with a Gaussian beam and a flat-top beam of 0.28 J/cm^2 fluence, as simulated using COMSOL Multiphysics. Femtosecond lasers generate a different heat distribution shape compared to nanosecond lasers due to their very short pulse width. This is because the pulse width is shorter than the heat transfer time from electrons to the lattice. Therefore, it is necessary to apply different formulas to electrons and lattice and use the electron-lattice coupling constant to accurately model the heat distribution [24,25].

$$C_e \frac{\partial T_e}{\partial t} = \frac{\partial}{\partial z}\left(k_e \frac{\partial T_e}{\partial z}\right) - g(T_e - T_l) + S \quad (1)$$

$$C_l \frac{\partial T_l}{\partial t} = \frac{\partial}{\partial z}\left(k_l \frac{\partial T_l}{\partial z}\right) + g(T_e - T_l) \quad (2)$$

$$S = I(x,t) * (1-R) * \alpha * \exp(-\alpha * y) \quad (3)$$

$$I(x,t) = I_0 * \exp\left(-\frac{x^2}{r^2}\right) * \exp\left(\frac{-3.5(t-\tau)^2}{\tau^2}\right) \quad (4)$$

$$C_e = \gamma T_e \quad (5)$$

$$k_e = k_0 \frac{T_e}{T_l} \quad (6)$$

Table 1. Summary of the major material properties used in calculations.

Parameter (unit)	Value
$\gamma\ (Jm^{-3}K^{-2})$	328.2
$k_0\ (Wm^{-1}K^{-1})$	22
$g\ (Wm^{-3}K^{-1})$	$13 * 10^{17}$
$C_l\ (Jm^{-3}K^{-1})$	$2.35 * 10^6$
$\tau\ (fs)$	190
$\alpha\ (cm^{-1})$	$4.8872 * 10^5$
Wavelength of the laser (*nm*)	1026
Target thickness (*nm*)	100
Target initial temperature (*K*)	300

Equation 1 represents the heat conduction formula applied to electrons, while Equation 2 represents the heat conduction formula applied to the lattice [10]. The parameters in these equations, denoted $\boldsymbol{C_e, C_l, k_e, k_l, g, S, R, \alpha}$ and $\boldsymbol{\tau}$ (see Table 1), correspond to the electron heat capacity, lattice heat capacity, electron thermal conductivity, lattice thermal conductivity, electron-photon coupling coefficient, laser source, reflectivity, absorption coefficient, and pulse duration, respectively [26-29]. Figures 4a and b show the heat distribution when a Ti sample is irradiated with a Gaussian beam and a flat-top beam, respectively, with the maximum temperature reached by the electrons at the center. The boundary conditions used in the COMSOL Multiphysics simulation were as follows. The left and right sides are set to be periodic condition, allowing for an infinitely extending and continuous domain. The top surface is in contact with air for cooling purposes. Between the air and the Ti material, convective heat flux is applied, resulting in heat transfer. The unit of the analyzed positions in figure 4 is meter. The Gaussian beam has a diameter of 12 µm, while the flat-top beam has a diameter of 10 µm. Figure 4a investigates the temperature change at the central area of the Gaussian beam (0,0) and the outer area of the beam (5E-6,0) to determine the heat distribution. The electrons at the (0,0) point in figure 4a reach a maximum temperature of 6,012 K, taking 0.41 ps to do so. Equilibrium between the electrons and the lattice is reached at 1,537 K, taking 2.6 ps. The electrons at the (5E-6,0) point in figure 4a reach a maximum temperature of 4,074 K, taking 0.39 ps to do so. Equilibrium between the electrons and the lattice is reached at 927 K, taking 1.88 ps. The temperature distribution is different at the center and the periphery due to the characteristics of the Gaussian beam profile. Since the melting point of Ti is 1,914 K, low fluence processing leads to a temperature distribution difference between the center and periphery, resulting in Gaussian-shaped processing [30,31]. As a result, homogeneous processing of a specific area is impossible, making it unsuitable for processing µ-LED TFTs. Figure 4b investigates the temperature change at the central area of the flat-top beam (0,0) and the outer area of the beam (4E-6,0) to determine the heat distribution. In figure 4b, at the (0,0) point, the electrons reach a maximum temperature of 4,374 K, taking 0.39 ps to do so. Equilibrium between the electrons and the lattice is reached at 1,014 K, taking 2.02 ps. At the (4E-6,0) point, the electrons reach a maximum temperature of 4,373 K, taking 0.39 ps to do so. Equilibrium between the electrons and the lattice is reached at 1,007 K, taking 1.96 ps. The maximum temperatures applied to the center and the periphery are almost the same due to the uniform intensity characteristics of the flat-top beam profile. Therefore, homogeneous processing is possible in both the center and the periphery, and a specific area can be processed into a square shape by adjusting the size of the slit.

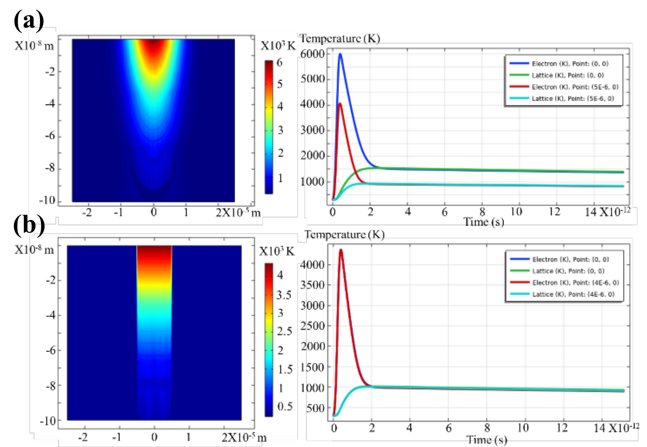

Fig. 4 Heat conduction distribution simulated by COMSOL Multiphysics. Gaussian and flat-top beams with 0.28 J/cm^2 fluence were irradiated at Ti 100 nm. Center and periphery temperature were analyzed. (a) Gaussian beam simulation, center point is located at (0, 0) and periphery point is located at (5E-6, 0). (b) Flat-top beam simulation, center point is located at (0, 0) and periphery point is located at (4E-6, 0).

Based on the data obtained in figure 4, a Ti thin film was processed using a flat-top beam with an irradiated fluence of 0.28 J/cm^2 in figure 5. Pulses of 1, 3, 5, and 7 were irradiated with 1 kHz repetition rate in figures 5a to d, and the change in processing characteristics that occurred when the number of pulses increased at the same fluence was investigated. As shown in figure 5f, the depth of ablation increased with the number of pulses, reaching a depth of about 50 nm in figure 5a and complete ablation of Ti 100 nm in figure 5d. In figure 5b, nucleation was observed with additional pulses [32]. Figure 5c showed a weak ripple phenomenon due to overlapping pulses, while figure 5d showed that only Ti was completely ablated, with no damage to the substrate. The use of a flat-top beam with a homogeneous beam profile minimized tensile strength in the center and periphery of the ablation area, resulting in minimal burrs, as shown in figure 5e. Unlike the burrs observed in figure 3a, almost no burrs were observed in figure 5e. The changes in depth observed in figures 5a to d are summarized in figure 5f.

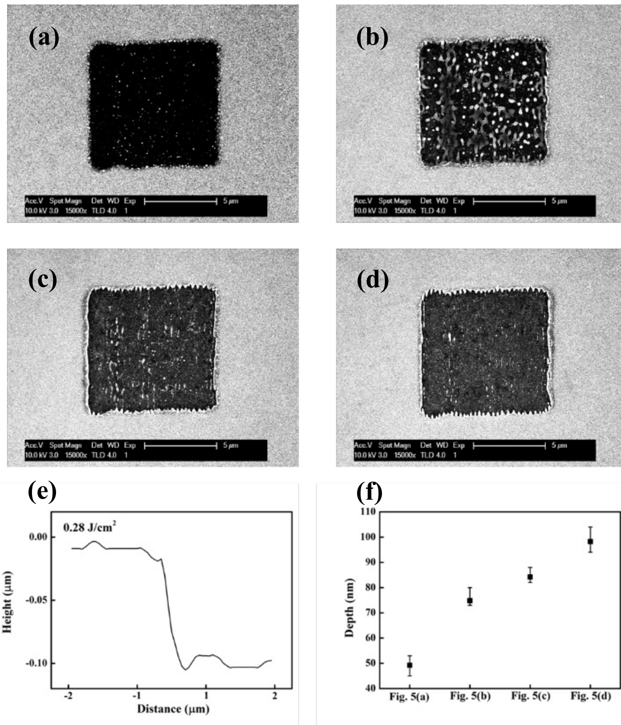

Fig. 5 SEM images of Ti surface after flat-top beam ablation. Flat-top beam with increasing number of pulses and 0.28 J/cm^2 fluence was irradiated to Ti 100 nm. (a) 1 pulse was irradiated. (b) 3 pulse was irradiated. (c) 5 pulse was irradiated. (d) 7 pulse was irradiated. (e) Representative morphology of flat-top beam ablation. (f) Depth of figure 5a, b, c, and d.

Figure 6 compares the morphology characteristics when using a Gaussian beam and a flat-top beam for processing at the same power, fluence, 1 kHz repetition rate, and 10 pulses. The use of 10 pulses suppresses the generation of ripples during irradiation. Figure 6a shows the processing at the same power ($0.28 * \mathbf{10^{-3}}$ W), and figure 6b shows the processing at the same fluence (0.28 J/cm^2) with a Gaussian beam based on Ti 100 nm processing with a flat-top of 0.28 J/cm^2 fluence in figure 6c. The fluence used in figure 6b (0.28 J/cm^2) is higher than that used in figure 6a (0.139 J/cm^2). As a result, the processing area was larger with a diameter of 10 μm in figure 6b and 8 μm in figure 6a. One notable difference between the two types of beams is that the processing area changes with the fluence of the Gaussian beam, while the processing area can be controlled using the size of the mechanical slit in the case of a flat-top beam. In figure 6d, we investigated the burr height of the processing areas in figures 6a, b, and c. We measured 10 random points on the left and right sides of the ablation area to determine the burr height. The burrs in figure 6a were higher than 40 nm on both sides, while the burrs in figure 6b were higher than 60 nm on both sides. However, the burrs in figure 6c were smaller than 20 nm on both sides. These results indicate that processing with a flat-top beam results in significantly lower burrs compared to processing with a Gaussian beam. Additionally, when using thicker samples, the burr height increases due to the increased amount of material pushed out by the tensile strength. In this case, the difference in burr height between the Gaussian beam and the flat-top beam is expected to be even greater.

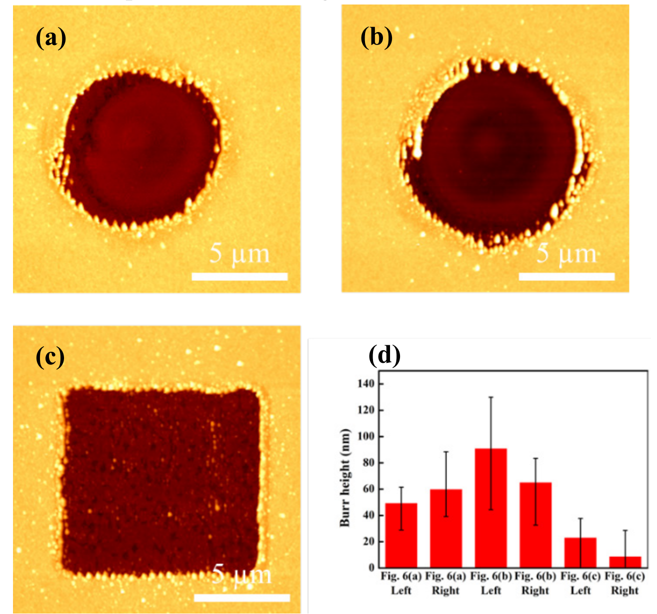

Fig. 6 AFM images and burr height analysis of ablation surface using Gaussian and flat-top beams. (a) and (c) have same power ($0.28 * 10^{-3}$ W). (b) and (c) have same fluence (0.28 J/cm^2). (a) 10 pulses of 0.139 J/cm^2 fluence Gaussian beam were irradiated. (b) 10 pulses of 0.28 J/cm^2 fluence Gaussian beam were irradiated. (c) 10 pulses of 0.28 J/cm^2 fluence flat-top beam were irradiated. (d) Left and right sides burr heights of figure 6a, b, and c were analyzed.

Figure 7 suggests the optimized conditions for ablating a Ti 100 nm film. Ti is a crucial material in the fabrication of μ-LED TFTs, and therefore appropriate processing is required to meet the demands of this application [4]. Since Ti is used in the form of a thin film in TFT, the processing characteristics of Ti 100 nm can be important in μ-LED TFT. Thus, a technology to completely remove the Ti thin film in a specific area is required, and the optimal processing conditions must be investigated in detail. This study aimed to determine the optimal processing conditions for completely ablating the Ti thin film while minimizing the occurrence of defects such as ripples and burrs. The optimal condition involved the use of a flat-top beam with a femtosecond pulse duration, an appropriate fluence of 0.28 J/cm2, and 7 pulses to ensure homogeneous processing while suppressing burr formation and avoiding ripple generation. Figure 5d confirms that 7 pulses did not generate ripples, and figure 5f shows that all 100 nm of the Ti film was ablated. Figure 6 demonstrates that the proposed laser condition resulted in lower burr formation compared to other conditions, using a flat-top beam with 0.28 J/cm2 fluence and 10 pulses. As a result, our proposed laser condition was able to completely remove the Ti 100 nm thin film in the desired area without generating ripples and minimizing burrs, which was confirmed through confocal microscopy, SEM, and AFM.

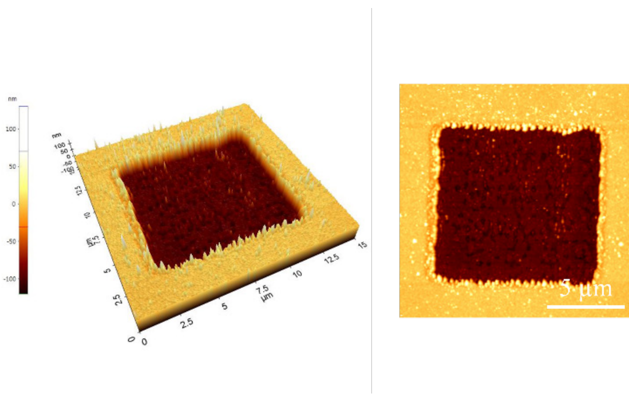

Fig. 7 AFM images of ablated Ti 100 nm without burr, ripple, substrate ablation. Flat-top beam with 0.28 J/cm^2 fluence and 7 pulses was irradiated.

In this study, ablation was conducted to minimize defects in a 100 nm thick Ti layer. These defects include burrs, ripples, and substrate ablation. Successful processing of the 100 nm Ti layer without encountering burrs, ripples, or substrate ablation was achieved. However, the specific thickness of the Ti thin films used in μ-LED varies among products. Therefore, the laser conditions required to minimize defects differ based on the sample type and thickness. To suppress burrs, a flat-top beam with 0.28 J/cm² energy density was employed. While using a flat-top beam effectively inhibited burr, excessively high fluence could induce burr. Therefore, for different types of samples, it is necessary to set lower or higher fluences to suppress burr. For ablation of the Ti 100 nm layer, seven pulses were applied. However, thicker samples require more pulses. To inhibit ripples, ablation should be carried out with the minimum number of pulses. To prevent substrate ablation, the laser should be irrdiated at a fluence that does not affect the underlying layer. Achieving minimized defect ablation for various sample types involves a detailed investigation of suitable laser conditions based on the principles mentioned above and simulations.

4. Conclusion

This study investigates the selective processing of Ti thin films used in TFTs of μ-LEDs, focusing on ablation with minimized defects in Ti 100 nm. In conventional laser processing, a target sample is processed using a Gaussian beam. However, burrs are formed by the Gaussian beam profile, ripples are induced when many pulses are irradiated, and substrates are ablated at the center of the laser when high fluences are irradiated. To suppress the formation of burrs, we simulated a flat-top beam with a square shape and the same intensity at the center and periphery using COMSOL Multiphysics. The simulation showed that the temperature change at the center and periphery of the beam was almost the same, indicating that homogeneous processing can be induced due to the characteristics of a homogeneous beam profile. In contrast, the temperature distribution of the Gaussian beam has a Gaussian profile, resulting in processing that follows a Gaussian form, with the central and peripheral regions irradiated with the laser exhibiting different ablation characteristics. Based on these characteristics, we processed Ti 100 nm using a small number of pulses, proper fluence, and a flat-top beam. As a result, ripple and burr were suppressed compared to processing with a Gaussian beam. The morphologies processed at the same power ($0.28 * \mathbf{10^{-3}}$ W) and fluence (0.28 J/cm^2) were compared to evaluate the efficacy of the flat-top beam, which showed superior suppression of burr formation. To ablate Ti 100 nm while minimizing defects, femtosecond pulse duration, 0.28 J/cm^2 fluence, 7 pulses, and flat-top beam are required. With these conditions, we homogeneously ablated Ti 100 nm while minimizing ripple and burr formation.

References

[1] Y. Huang, E. L. Hsiang, M. Y. Deng, and S. T. Wu: Light Sci. Appl., 9, (2020) 105.
[2] T. Wu, C. W. Sher, Y. Lin, C. F. Lee, S. Liang, Y. Lu, S. W. H. Chen, W. Guo, H. C. Kuo, and Z. Chen: Appl. Sci., 8, (2018) 1557.
[3] Y. Huang, G. Tan, F. Gou, M. C. Li, S. L. Lee, and S. T. Wu: J. Soc. Inf. Disp., 27, (2019) 387.
[4] J. H. Choi, S. J. Lee, K. O. Kwon, J. Y. Choi, T. Jung, M. Han, and S. J. Han: Appl. Phys. Express., 13, (2020) 026501.
[5] B. N. Chichkov, C. Momma, S. Nolte, F. von Alvensleben, and A. Tünnermann: Appl. Phys. A., 63, (1996) 109.
[6] S. Nolte, C. Momma, H. Jacobs, A. Tünnermann, B. N. Chichkov, B. Wellegehausen, and H. Welling: J. Opt. Soc. Am. B., 14, (1997) 2716.
[7] K. Sugioka and Y. Cheng: Appl. Phys. Rev., 1, (2014) 041303.
[8] Y. G. Shin, W. Choi, J. Choi, and S. H. Cho: J. Micro. Nanomanuf., 9, (2021) 041002.
[9] Y. G. Shin, S. Y. Ji, J. Choi, and S. H. Cho: Appl. Phys. A., 128, (2022) 828.
[10] Y. G. Shin, J. Choi, and S. H. Cho: Int. J. Precis. Eng., (2023) 1.
[11] J. Bonse, S. Höhm, S. V. Kirner, A. Rosenfeld, and J. Krüger: IEEE J. Sel. Top. Quantum Electron., 23, (2016) 9000615.
[12] M. Huang, F. Zhao, Y. Cheng, N. Xu, and Z. Xu: ACS Nano., 3, (2009) 4062.
[13] J. Bonse, A. Rosenfeld, and J. Krüger: J. Appl. Phys., 106, (2009) 104910.
[14] H. Y. Kim, W. S. Choi, S. Y. Ji, Y. G. Shin, J. W. Jeon, S. Ahn, and S. H. Cho: Appl. Phys. A., 124, (2018) 1.
[15] H. Y. Kim, J. W. Yoon, W. S. Choi, K. R. Kim, and S. H. Cho: Opt. Lasers Eng, 84, (2016) 44.
[16] R. Le Harzic, D. Breitling, M. Weikert, S. Sommer, C. Föhl, S. Valette, C. Donnet, E. Audouard, and F. Dausinger: Appl. Surf. Sci., 294, (2005) 322.
[17] A. Rodríguez, M. C. M. Miñana, A. D. Ponte, M. M. Calderón, M. G. Aranzadi, and S. M. Olaizola: Appl. Surf. Sci., 351, (2015) 135.
[18] T. T. D. Huynh and N. Semmar: Appl. Phys. A., 116, (2014) 1429.
[19] J. Cheng, W. Perrie, M. Sharp, S. P. Edwardson, N. G. Semaltianos, G. Dearden, and K. G. Watkins: Appl. Phys. A., 95, (2009) 739.
[20] C. Cheng and X. Xu: Phys. Rev. B., 72, (2005) 165415.

[21] J. P. Colombier, P. Combis, R. Stoian, and E. Audouard: Phys. Rev. B., 75, (2007) 104105.
[22] F. Korte, S. Nolte, B. N. Chichkov, T. Bauer, G. Kamlage, T. Wagner, C. Fallnich, and H. Welling: Appl, Phys. A., 69, (1999) S7.
[23] Y. Gan and J. K. Chen: J. Appl. Phys., 108, (2010) 103102.
[24] Z. Han, C. Zhou, E. Dai, and J. Xie: Opt. Commun. 281, (2008) 4723.
[25] S. S. Wellershoff, J. Hohlfeld, J. Güdde, and E. Matthias: Appl. Phys. A., 69, (1999) S99.
[26] X. Wang, W. Ye, H. Yao, P. Wei, F. Yin, J. Cong, Y. Tong, L. Zhang, and W. Zhu: J. Laser. Appl., 33, (2021) 012047.
[27] D. Liu, C. Chen, B. Man, X. Meng, Y. Sun, and F. Li: Eur. Phys. J. Appl. Phys., 72, (2015) 31301.
[28] P. B. Johnson and R. W. Christy: Phys. Rev. B., 9, (1974) 5056.
[29] M. Watanabe, M. Adachi, and H. Fukuyama: J. Mol. Liq., 324, (2021) 115138.
[30] K. A. Gschneidner Jr: Solid. State. Phys., 16, (1964) 275.
[31] D. A. Young : “Phase diagram of the elements” ed. by California University (Publisher, USA, 1975) p.18.
[32] N. Maharjan, W. Zhou, Y. Zhou, and Y. Guan: Appl. Phys. A., 124, (2018) 1.

(Received: May 15, 2023, Accepted: October 8, 2023)